

Gradient-index electron optics in graphene p - n junctions

Emmanuel Paredes-Rocha^{1,*}, Yonatan Betancur-Ocampo^{1,†}, Nikodem Szpak^{2,‡} and Thomas Stegmann^{1,§}

¹*Instituto de Ciencias Físicas, Universidad Nacional Autónoma de México, Cuernavaca, México*

²*Fakultät für Physik, Universität Duisburg-Essen, Duisburg, Germany*



(Received 23 September 2020; revised 26 November 2020; accepted 30 November 2020; published 7 January 2021)

We investigate the electron transport in smooth graphene p - n junctions, generated by gradually varying electrostatic potentials. The numerically calculated coherent current flow patterns can be understood largely in terms of semiclassical trajectories, equivalent to the ones obtained for light beams in a medium with a gradually changing refractive index. In smooth junctions, energetically forbidden regions emerge, which increase reflections and can generate pronounced interference patterns, for example, whispering gallery modes. The investigated devices do not only demonstrate the feasibility of the gradient-index electron optics in graphene p - n junctions, such as Luneburg and Maxwell lenses, but may have also technological applications, for example, as electron beam splitters, focusers, and waveguides. The semiclassical trajectories offer an efficient tool to estimate the current flow paths in such nanoelectronic devices.

DOI: [10.1103/PhysRevB.103.045404](https://doi.org/10.1103/PhysRevB.103.045404)

I. INTRODUCTION

The ballistic, beamlike propagation of electrons in graphene enables the observation of optical-like phenomena in this material. This electron optics has recently come into focus of research with several theoretical and experimental contributions [1–16]. For example, it has been shown that an electron beam, which hits the interface of a graphene p - n junction, behaves like a light beam at the interface of two materials with different refractive indices. Hence, the reflection and refraction of the electrons follows a generalized version of Snell's law, where the refractive indices are determined by the electrostatic potential in the p and n regions of the junction [1,6,9,10,17–19]. Due to the special dispersion relation of graphene, negative reflection can be observed, a property that has been seen before only in the light propagation in metamaterials [20–22]. Moreover, Klein tunneling—the absence of backscattering at normal incidence—is observed, which can be attributed to the pseudospin conservation of the electrons in graphene. It has also been shown that an electron beam in graphene can be deflected by means of elastic deformations that induce a strong pseudomagnetic field [23–28].

The possibility to manipulate electron beams in graphene by means of p - n junctions or elastic deformations has led to various proposals for nanoelectronic devices, such as Veselago lenses [4,6,29–35], electron fiber optics [3,36], interferometers [37,38], valley beam splitters [7,26,39–50], collimators [51,52], switches [53], reflectors [54,55], transistors [2,56,57], and Dirac fermions microscopes [58]. Electron optics has been extended recently from graphene to other

materials, such as phosphorene, where negative reflection has been predicted [59,60], noncoplanar refraction and Veselago lenses in Weyl semimetals [61–64], anomalous caustics in borophene p - n junctions [65], and superdiverging lenses in Dirac materials [30].

Most of the work on electron optics in graphene p - n junctions involves interfaces where the electrostatic potential (and hence the refractive index) changes abruptly [8,29,35,66–68]. Recent experiments have demonstrated that such abrupt junctions can indeed be realized [13]. P - n junctions with a smoothly changing electrostatic potential are often regarded as disadvantageous, because they induce an energetically forbidden region and hence reduce the transmission. Nevertheless, one can also take advantage of the reduced transmission to construct quantum dots based on smooth circular p - n junctions. These junctions show interesting physical properties like Mie scattering [29] and whispering gallery modes [69]. They have been realized recently in experiments [4,70].

A smoothly changing electrostatic potential can be understood as a smoothly changing refractive index that establishes gradient-index optics. In this paper, we investigate to which extent graphene p - n junctions show gradient-index optics phenomena. We will study straight p - n junctions as well as circular junctions which have received little attention so far. On the one hand side, we will calculate numerically the current flow in these systems, applying the nonequilibrium Green's function method to the tight-binding model. On the other hand side, using the geometric optics approximation, we will determine the semiclassical trajectories of the electron beams. Comparing both approaches, we will show that they agree in a wide regime of parameters. Nevertheless, discrepancies emerge which can be explained by the interference of electron waves. These wave effects increase for smooth circular junctions as they can partially confine the electron beam.

*eparedes@icf.unam.mx

†ybetancur@icf.unam.mx

‡nikodem.szpak@uni-due.de

§stegmann@icf.unam.mx

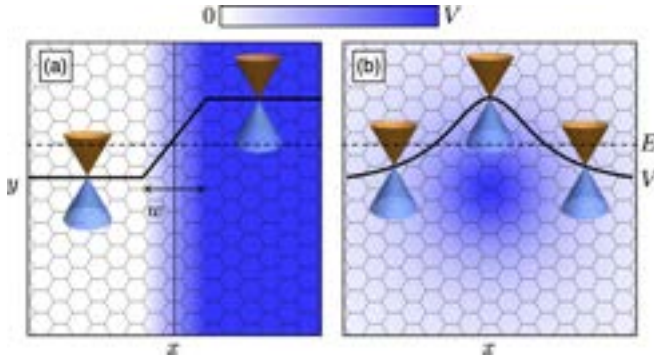


FIG. 1. Straight (a) and circular (b) graphene p - n junctions. The bluish color shading shows the electrostatic potential within the graphene ribbon. Both junctions have a smooth interface that separates the two regions of different doping. The profile of the electrostatic potential is indicated by the solid black lines, which shifts locally the conical energy bands of graphene. This causes that the electrons at energy E (black dashed lines) go from the conduction band (orange cone) to the valence band (light blue cone).

II. SYSTEM AND METHODS

A. Graphene p - n junctions

We model the electronic structure of graphene by the tight-binding Hamiltonian

$$H = -t \sum_{i,j} |i^A\rangle \langle j^B| + \text{H.c.}, \quad (1)$$

which describes well the electron transport at low energies. The $|i^{A/B}\rangle$ indicate the atomic states localized on the carbon atoms at positions \mathbf{r}_i on the sublattices A and B, respectively. The sum runs over nearest neighboring atoms, which are separated by a distance of $a = 0.142$ nm and coupled with the energy $t = 2.8$ eV. A plane-wave ansatz leads at low energies to the continuous Dirac Hamiltonian

$$H_{\text{Di}}^{\pm}(\mathbf{k}) = \hbar v_F \boldsymbol{\sigma}_{\pm} \cdot \mathbf{k}, \quad (2)$$

at the two Dirac points $\mathbf{K}_{\pm} = (0, \pm 4\pi/(3\sqrt{3}a))$ at the edges of the Brillouin zone. The wave vector \mathbf{k} is measured with respect to these Dirac points. We define $\hbar v_F = 3at/2$ and $\boldsymbol{\sigma}_{-} = \boldsymbol{\sigma}_{+}^{*} = (\sigma_1, \sigma_2)$. The valley degree of freedom of the electrons in graphene, which may be used for a new kind of electronics called valleytronics [41,43–48], will not be relevant in the present work, because the considered p - n junctions do not affect it. The Dirac Hamiltonian leads to the well-known conical energy bands of graphene

$$E(\mathbf{k}) = s\hbar v_F |\mathbf{k}|, \quad (3)$$

where $s = \text{sgn}(E) = \pm 1$ is the band index.

A graphene p - n junction is constituted by regions of different doping; see Fig. 1. Such regions can be generated by metallic gates that induce an electrostatic potential, $V(\mathbf{r})$, in the continuous space representation or $V = \sum_i V_i |i\rangle \langle i|$ in the tight-binding approach. This potential shifts the energy bands of graphene and hence generates a junction. A p - n junction is generated if the electrons go from one band to another through interband tunneling, while in a p - p' or n - n' junction intraband tunneling takes place within the valence or conduction band,

respectively. In the following, we will concentrate on straight p - n junctions [Fig. 1(a)], generated by the electrostatic potential

$$V_{\text{lin}}(\mathbf{r}) = \begin{cases} 0 & \text{if } x \leq -w/2 \\ \left(\frac{x}{w} + \frac{1}{2}\right)V & \text{if } |x| < w/2 \\ V & \text{if } x \geq w/2 \end{cases} \quad (4)$$

and circular junction [Fig. 1(b)] with the potential

$$V_{\text{cir}}(\mathbf{r}) = \frac{V}{1 + (r/r_0)^{\alpha}}. \quad (5)$$

The smoothness¹ of the p - n junctions is controlled by the parameters w and α . Note that circular p - n junctions can be also understood as p - n - p junctions. Such p - n junctions, straight and circular ones, have been realized experimentally; see, for example, Refs. [1,4,10,13,69–71].

B. Semiclassical trajectories

Within semiclassical theory, the propagation of the electron wave functions is approximated by the propagation of point particles. In order to apply this approximation to the quantum system described by the Dirac Hamiltonian, Eq. (2), we use the eikonal approximation and the methods developed in Ref. [26] to obtain relativistic trajectories (geodesics) for massless particles coupled to the electric potential $V(\mathbf{r})$

$$\frac{d\mathbf{p}}{dt} \equiv \frac{d}{dt} \left(\frac{[E - V(\mathbf{r})] d\mathbf{r}}{v_F^2} \right) = -\nabla V(\mathbf{r}), \quad (6)$$

where the momentum vector $\mathbf{p}(t)$ along the trajectory $\mathbf{r}(t)$ satisfies the dispersion relation $[E - V(\mathbf{r})]^2 = v_F^2 \mathbf{p}^2$. This approach is discussed in detail in our previous works and applied successfully to understand the current flow paths in elastically deformed graphene [26,39].

In order to get additional insight, the dynamics can be reformulated by means of the classical pseudorelativistic Hamiltonian

$$H_{\text{sc}} = s(\mathbf{r}) v_F |\mathbf{p}| + V(\mathbf{r}), \quad (7)$$

where $s(\mathbf{r}) = \text{sgn}(E - V(\mathbf{r}))$ is the band index and $|\mathbf{p}| = \sqrt{p_x^2 + p_y^2} = \sqrt{p_r^2 + p_{\theta}^2/r^2}$ is the momentum in Cartesian and polar coordinates, respectively. The trajectories of the ballistic electrons described by this Hamiltonian can be related to optical rays in an artificial medium with the refractive index

$$n(\mathbf{r}) \equiv \frac{E - V(\mathbf{r})}{v_F}. \quad (8)$$

Taking into account that the electrostatic potential $V(\mathbf{r})$ can change smoothly (on the length scale defined by the Fermi wavelength of the electrons), we obtain in this way a gradient-index medium.

¹Note that mathematical smoothness is not relevant here.

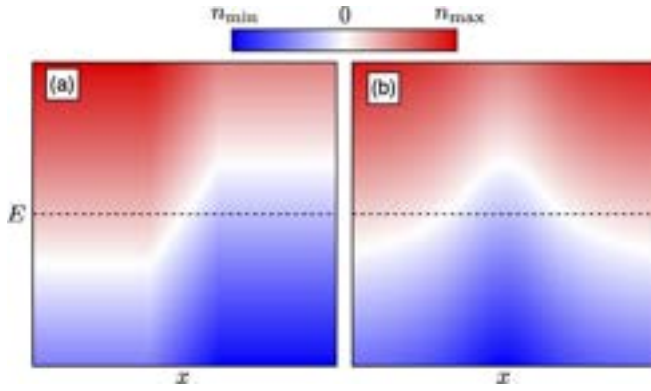


FIG. 2. Refractive index n in a straight (a) and circular (b) graphene p - n junction as a function of the position x [compare Fig. 1] and the electron energy E . Reddish colors indicate $n > 0$, while bluish colors represent $n < 0$. Note that for certain electron energies (dashed horizontal line) n changes its sign in the narrow white region.

The equations of motion in a straight junction are given by

$$\begin{aligned} \frac{dx}{dt} &= \partial_{p_x} H = \frac{s(x) v_F p_x}{\sqrt{p_x^2 + p_y^2}} = \frac{v_F p_x}{n(x)}, \\ \frac{dy}{dt} &= \partial_{p_y} H = \frac{s(x) v_F p_y}{\sqrt{p_x^2 + p_y^2}} = \frac{v_F p_y}{n(x)}. \end{aligned} \quad (9)$$

Eliminating the time dependency by dividing both expressions, we obtain for the semiclassical trajectories

$$y(x) = y_0 + p_y \int_{x_0}^x \frac{s(x') dx'}{\sqrt{n^2(x') - p_y^2}}, \quad (10)$$

where $\mathbf{r}_0 = (x_0, y_0)$ is the initial position of the electron. A similar analysis for the electron trajectories in circular junctions leads to

$$\theta = \theta_0 + l \int_{r_0}^r \frac{s(r') dr'}{r' \sqrt{r'^2 n^2(r') - l^2}}, \quad (11)$$

where $l \equiv p_\theta$ is the angular momentum. Note that the momentum component p_y is conserved in straight junctions due to the translational symmetry along the y axis [see Fig. 1(a)], while the angular momentum $\equiv p_\theta$ is conserved in circular junctions due to the rotational symmetry [see Fig. 1(b)].

These electron trajectories are identical to the ones obtained for light beams in gradient-index optics [72], apart from an important difference: The refractive index $n(\mathbf{r})$ depends on the electron energy and changes its sign when the electrons go from the conduction (n region) to the valence band (p region); see Fig. 2. It is all negative for p - p' and positive for n - n' junctions. Moreover, the square root in the denominator of Eqs. (10) and (11) can become imaginary in certain regions of the system, which are defined by the inequalities $|n(x)| \leq |p_y|$ and $|n(r)| \leq |l|/r$ for straight and circular junctions, respectively. These forbidden regions are indicated in Fig. 3 by those ranges where the refractive index (bluish-reddish curve) lies in the gray-shaded regions. While classically those regions

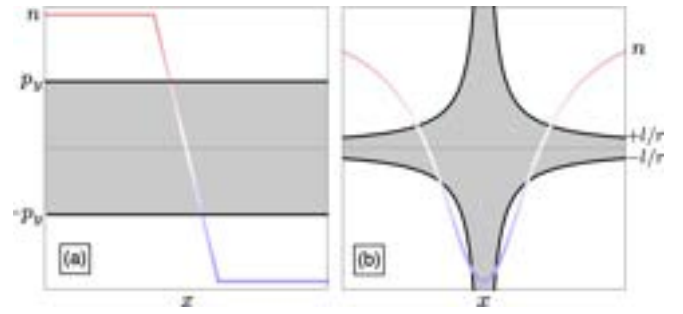


FIG. 3. The reddish-bluish curve gives the refractive index n at constant electron energy, see the dashed horizontal curves in Fig. 2. The black curves represent the momentum component p_y and l in straight (a) and circular (b) junctions, respectively. When n is in the gray shaded regions, the root in Eqs. (10) and (11) is imaginary and the electrons have to tunnel through a forbidden region.

cannot be penetrated, quantum mechanically the electrons can tunnel through the forbidden regions.

As tunneling is largely suppressed in smooth junctions, the boundary of the forbidden region defines the reflection zone for the beam. Figure 3 explains that the transmission decreases if the incidence of the electrons becomes more oblique, because p_y (or l) increases and, thereby, the size of the forbidden region increases, too. In the same way, the transmission is perfect for normal incidence, because $p_y = 0$ (or $l = 0$) and the forbidden region disappears, which matches with the pseudospin conservation. The semiclassical trajectories obtained from the geometrical optics are equivalent to the relativistic geodesics in the classical region ($n > 0$), but offer additional techniques to deal with nonclassical phenomena like tunneling through classically forbidden regions. Note also that the refractive index in Fig. 2(b) is astonishingly similar to a measurement of the local resistance in Ref. [4].

C. The nonequilibrium Green's function method for the current flow

The current flow in the graphene p - n junction is calculated by means of the nonequilibrium Green's function (NEGF) method. This quantum method is based on the tight-binding Hamiltonian, Eq. (1). It does not rely on the approximations made in the previous section to obtain the semiclassical trajectories and thus allows us to verify their validity. As the NEGF method is discussed in detail in various textbooks [see, e.g., Refs. [73,74]], we summarize here only briefly the essential formulas.

The Green's function of the system is given by

$$G(E) = (E - H - V - \Sigma)^{-1}, \quad (12)$$

where E is the energy of the injected electrons, H is the tight-binding Hamiltonian, Eq. (1), and V is the electrostatic potential. In order to suppress boundary effects and mimic an infinite system, we place a constant complex potential $\Sigma = -i \sum_{j \in \text{edges}} |j\rangle \langle j|$ at the edges of the system, which should absorb the electrons.

The electrons are injected at the left edge of the system as plane waves propagating toward the interface of the p - n junction. Their momentum is determined by the electron

energy, Eq. (3), and the angle of injection $\theta = \arctan k_y/k_x$. This injection is represented by the in-scattering function

$$\Sigma^{\text{in}} = \sum_{i,j \in \text{edge}} A(\mathbf{r}_i) A(\mathbf{r}_j) \psi_j^*(\mathbf{k}) \psi_i(\mathbf{k}) |i\rangle \langle j|, \quad (13)$$

where the sum runs over all carbon atoms at the left system edge; see Fig. 1. The $\psi_i(\mathbf{k})$ are the eigenstates of the Dirac Hamiltonian, Eq. (2),

$$\psi_j(\mathbf{k}) = \begin{cases} c^- e^{i(\mathbf{k}+\mathbf{K}^-)\mathbf{r}_j} + c^+ e^{i(\mathbf{k}+\mathbf{K}^+)\mathbf{r}_j} & j \in A, \\ s c^- e^{i(\mathbf{k}+\mathbf{K}^-)\mathbf{r}_j + i\phi} - s c^+ e^{i(\mathbf{k}+\mathbf{K}^+)\mathbf{r}_j - i\phi} & j \in B, \end{cases} \quad (14)$$

where $\phi = \arg(ik_x + k_y)$. The parameters c^\pm control the occupation of the two \mathbf{K}^\pm valleys. We consider the case in which both valleys are fully mixed, i.e., $c_\pm = \pm 1/2$. The function

$$A(\mathbf{r}) = e^{-(y-y_0)^2/d_0^2} \quad (15)$$

gives the injected current beam a Gaussian profile. The parameters y_0 and d_0 control the position and width of the beam. We will see later that this model allows us to inject ballistic electron beams in graphene.

Finally, the current flowing between the atoms at positions \mathbf{r}_i and \mathbf{r}_j is calculated by

$$I_{ij} = \text{Im}(t G \Sigma^{\text{in}} G^\dagger)_{ij}. \quad (16)$$

This bond current is averaged (or coarse-grained) over the six edges of the carbon hexagons. This current vector field is visualized in the following [see, for example, Fig. 4(a)] by means of yellow arrows. Its norm, the current density, is represented by the red color shading.

Good agreement between the quantum current flow and the semiclassical trajectories of geometric optics can be expected only in the specific parameter regime, where the Fermi wavelength of the electrons λ_F is much larger than the interatomic distance a but smaller than the system size (L_x, L_y). Moreover, smooth changes of the electrostatic potential, as sketched in Fig. 1, can be resolved only if the Fermi wavelength is shorter than the spatial variations of the potential $\Delta_{x/y} V$. These conditions can be summarized in the inequality

$$a \ll \lambda_F = \frac{2\pi}{|k|} < \Delta_{x/y} V \ll L_{x/y}. \quad (17)$$

However, when the electrostatic potential changes smoothly, the effective electron energy $E - V$, and hence the Fermi wavelength, will change, which may lead to a local violation of the inequality.

III. RESULTS

A. Straight graphene p - n junctions

We begin our discussion by analyzing the current flow in a homogeneous graphene nanoribbon with a size of about 150×150 nm or larger.² In Fig. 4(a), electrons are injected according to Eq. (13) at the left ribbon edge with energy $E = 0.15t \approx 420$ meV (corresponding to the Fermi wavelength $\lambda_F \approx 9$ nm) and a momentum vector parallel to the horizontal

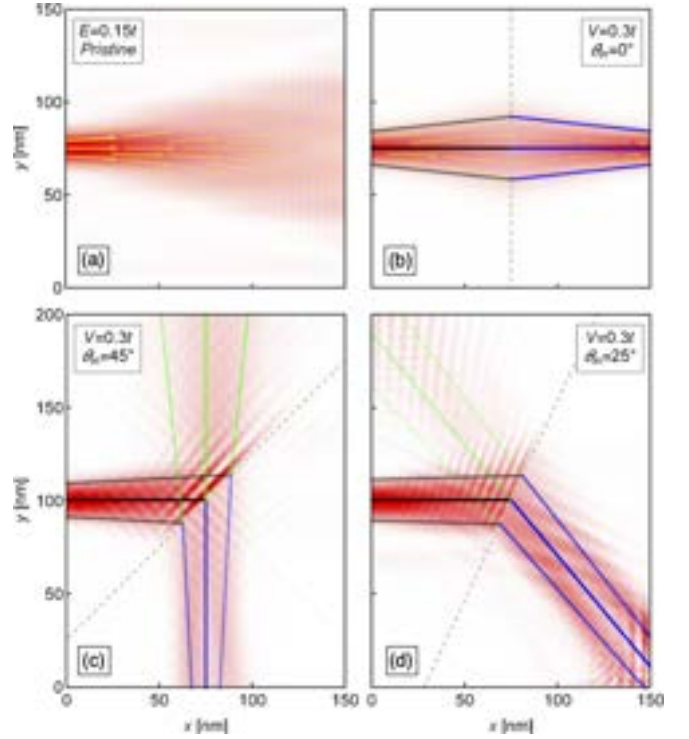


FIG. 4. Current flow in a graphene nanoribbon in the absence (a) and presence [(b)–(d)] of an electrostatic potential which changes abruptly at the dashed line and hence generates a p - n junction. The current density is indicated by the red color shading and the current vector field by yellow arrows. The diverging electron beam in panel (a) is refocused by the p - n junction in (b). The semiclassical trajectories from Eq. (10) [see the solid black, blue, and green lines] agree with the current flow patterns calculated by means of the NEGF method. At the interface of the p - n junction, the electron beam is split into a reflected and transmitted electron beam, in agreement with the generalized Snell's law, Eq. (18).

x axis. A beamlike propagation of the electrons with some divergence due to diffraction is observed, which will enable us to compare the numerically calculated current flow patterns with the semiclassical trajectories.

In Fig. 4(b), a straight p - n junction is introduced by an electrostatic potential which changes abruptly from zero to the constant value $V = 2E$ at the dashed line. We observe negative refraction at the interface of the p - n junction, which refocuses the electron beam. Moreover, Klein tunneling, i.e., the absence of back-scattering at normal incidence, occurs. When the junction is tilted,³ the electrons do not hit the interface orthogonally and the incident electron beam is split into a reflected and refracted beam. The solid black, blue, and green lines in Fig. 4 are the predicted semiclassical trajectories [Eq. (10)] for the incident, transmitted, and reflected electron beams, respectively. They follow a generalized Snell's law,

$$\theta_{\text{re}} = -\theta_{\text{in}} \quad \text{and} \quad \frac{\sin(\theta_{\text{in}})}{\sin(\theta_{\text{tr}})} = \frac{n_{\text{tr}}}{n_{\text{in}}} = \frac{E - V}{E}, \quad (18)$$

²The accuracy of the used approximations increases with the system size.

³Note that due to the isotropy of graphene's electronic structure at low energies, tilting the junction is equivalent to injecting the electrons under a different angle.

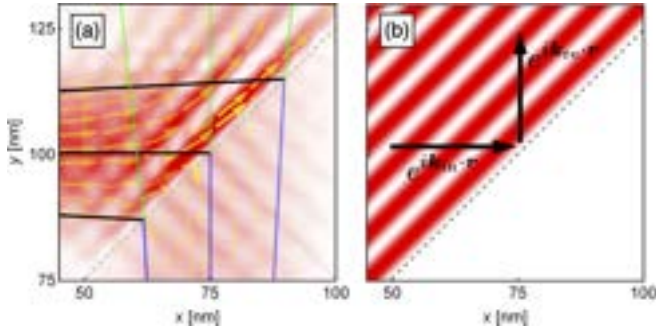


FIG. 5. Current flow close to the interface of the graphene p - n junction. (a) Enlargement of the interface region of Fig. 4(c). (b) Probability density generated by the superposition of the incoming and reflected electron beam, $|e^{ik_{in} \cdot r} + e^{ik_{re} \cdot r}|^2$. The good agreement in panels (a) and (b) shows that the interference between the two electron beams generates the ripple pattern.

where $\theta_{in/tr/re}$ are the angles of incidence, transmission, and reflection, while $n_{in/tr}$ as defined in Eq. (8) take the roles of the refractive indices in the n and p regions, respectively. In general, these trajectories agree very well with the numerical quantum calculations; see Figs. 4(b)–4(d). Electron optics in such straight p - n junctions has been studied largely before [1,2,6–11,14–16,18,19,53,56,58,66,71,75]. Here, we have confirmed the generalized Snell's law by means of numerical quantum calculations of the current flow. Additionally, we observe in Figs. 4(c) and 4(d) a ripple pattern close to the interface of the p - n junction, magnified in Fig. 5(a). In Fig. 5(b), we show the superposition of the incoming and reflected electron wave, $|e^{ik_{in} \cdot r} + e^{ik_{re} \cdot r}|^2$. The agreement of both figures confirms that the ripples are an interference effect of the electron wave functions, which goes beyond semiclassical trajectories. Similar ripple patterns can also be observed close to the edges of the graphene nanoribbon. They can be explained in the same way by the reflections at the system boundary. The absorption of the electrons at the edges by the complex potential is not perfect and hence generates a small reflected part which interferes with the incoming beam. We can also observe in Fig. 5(a) that the current changes its direction not instantaneously at the interface of the junction but in a finite region due to the finite width of the incident electron beam. This effect is not covered by the semiclassical trajectories, which have zero width.

We continue our discussion with smooth graphene p - n junctions, where the electrostatic potential changes linearly over a width of $w = 350a \approx 50 \text{ nm} \approx 5\lambda_F$; see Fig. 1(a). As shown in Fig. 6, the semiclassical trajectories agree well with the current density obtained by means of the NEGF method. The generalized Snell's law remains valid for such smooth junctions. However, in comparison with the case of an abruptly changing potential [see Fig. 4], a much larger part of the incident current is reflected. This effect can be observed even for normal incidence, where Klein tunneling takes place due to the diffraction of the electron beam which slightly changes the propagation direction. The effect gets even more pronounced for narrower electron beams for which the diffraction is stronger; compare Figs. 6(a) and 6(b). Such p - n junctions can be used to generate narrow parallel electron beams.

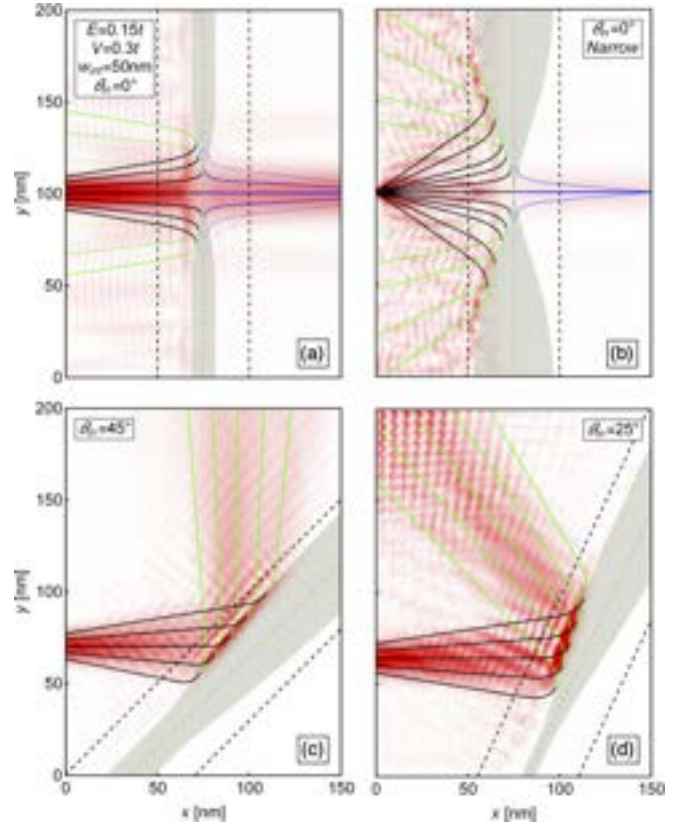


FIG. 6. Current flow in a straight graphene p - n junction with a smoothly changing profile ($w \approx 50 \text{ nm}$). The width of the junction is indicated by dashed black lines [see Fig. 1(a)]. The points where the electrons go from the conduction to the valence band are indicated by a gray dashed line. The semiclassical trajectories (solid lines) agree well with the NEGF current density (red color shading). The forbidden region is indicated by the gray shaded region. At the edge of this region, the current density accumulates and the semiclassical trajectories return. Note that the forbidden zone in the case of normal incidence [(a), (b)] appears due to the diffraction of the electron beam, which has been determined on the basis of Fig. 4(a).

The increasing reflection can be understood by the rise of the forbidden zone [see Fig. 3(a)], which is indicated in Fig. 6 by the gray shaded regions. Moreover, an accumulation of the current density can be observed just at the edge of the forbidden zone, which coincides with the point of return of the semiclassical trajectories. Note that we have also sketched trajectories in the forbidden regions by using the substitution $\mathbf{k} \rightarrow i\mathbf{k}$, which converts evanescent waves to propagating ones. Although the Fermi wavelength diverges in this region and the geometric approximation might break down the continuation of the trajectories to another classical region agrees again very well with the quantum current.

Until now, we have discussed only the case of p - n junctions, where interband tunneling occurs. In the case of n - n' and p - p' junctions, the electrons remain in the same band and the current flow patterns change qualitatively. In Fig. 7, a narrow (and hence strongly diverging) electron beam is injected at the left ribbon edge. In contrast to the p - n junction [see Fig. 6(b)], the current is largely transmitted through the interface of the junction. Moreover, in the n - n' junction [Fig. 7(a)],

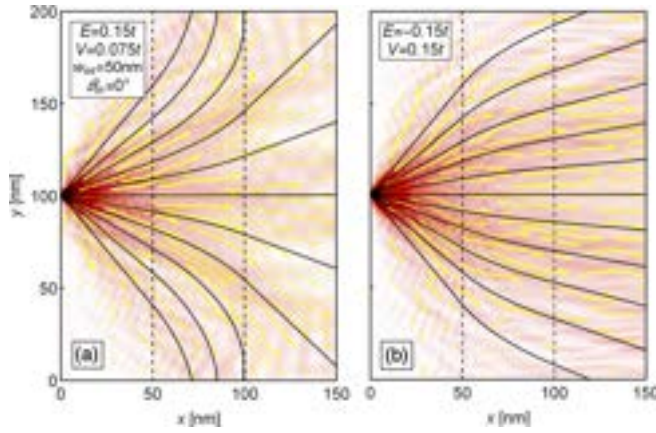


FIG. 7. Electron optics in a smooth n - n' (a) and p - p' (b) junctions. The electrons are injected as a very narrow beam with strong diffraction. The current is transmitted largely through the junction in contrast to the p - n junction, where the electrons are transmitted only at normal incidence [compare Fig. 6(b)].

the divergence of the electron beam is enhanced, whereas in the p - p' junction [Fig. 7(b)], it is reduced similarly to a converging lens. Note that in n - n' junctions a critical angle exists, beyond which total reflection occurs; see the outermost trajectories in Fig. 7(a).

B. Circular graphene p - n junctions

Let us consider now the circular graphene p - n junctions. As in the case of straight junctions, we begin with an abruptly changing electrostatic potential, obtained by $\alpha \rightarrow \infty$ in Eq. (5). In Fig. 8, it can be observed that a part of the current density is deflected around the p - n junction, while the part that enters the junction is focused onto a single point [5]. The semiclassical trajectories show a caustic inside the junction, in agreement with the focusing point observed in the current density. However, outside the junction both approaches are much less in line. This disagreement can be explained by the

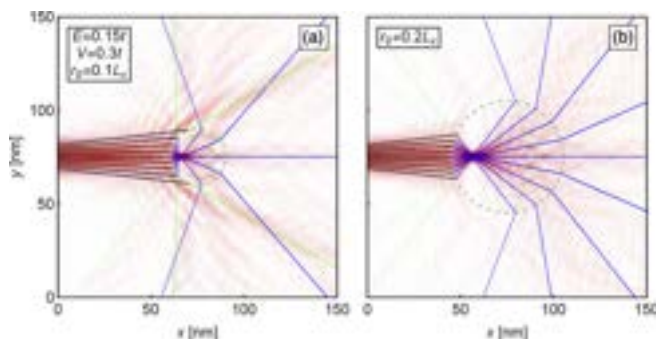


FIG. 8. Current flow in a circular graphene p - n junction. The electrostatic potential is changing abruptly at the dashed circle from zero to $V = 2E$. A single focusing point emerges inside the junction, whose interface is denoted by the dashed circle. Outside the junction, the electrons are scattered divergently. The semiclassical trajectories agree well with the current flow inside the junction, but not that well outside due to interference of the incoming and reflected electron waves in a wide region.

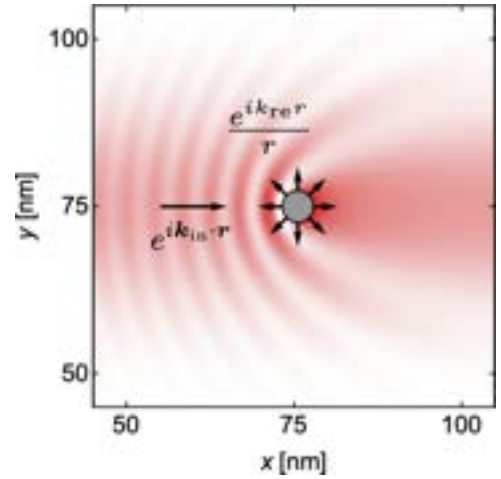


FIG. 9. Interference of an incoming plane wave [with Gaussian profile; see Eq. (15)] and a reflected circular electron beam, $|A(\mathbf{r})e^{ik_{in} \cdot \mathbf{r}} + e^{ik_{re} \cdot \mathbf{r}}/r|^2$ shows that the current pattern outside the junction is changed strongly by interference.

wave nature of the electrons, which leads in straight junctions to a ripple pattern at the interface of the junction due to the interference between the incoming and reflected electron waves. In circular junctions, the reflected electron wave is (approximately) circular and hence interferes with the incident wave in a much larger region. The resulting interference pattern shown in Fig. 9 agrees qualitatively with the observed current pattern and demonstrates the limitations of the geometric optics in circular p - n junctions. Additionally, we note in Fig. 8 that when the radius of the junction is reduced, the incidence of lateral electrons becomes more grazing and a larger part of the electrons is deflected around the junction.

By smoothing the profile of the electrostatic potential ($\alpha = 2$), we obtain a circular junction with a gradually changing refractive index, which is certainly the most appealing device for gradient-index electron optics. Such a device has been realized recently experimentally [4,70]. Current flow patterns are shown in Fig. 10 together with semiclassical trajectories, which agree roughly with the quantum current. The disagreement can be explained by strong interference due to an energetically forbidden region through which the electrons have to tunnel. Therefore, a large fraction of the incident electron beam is reflected, which causes a ripple pattern that is much more pronounced than in abrupt circular junctions; see Fig. 8. Similar to smooth straight junctions [see Fig. 6], an accumulation of the current density can be observed at the edges the forbidden region, which is indicated in the semiclassical trajectories by a color change from black to green. The size of the forbidden region is minimal for the electrons of normal incidence [see Fig. 3] and hence, those electrons enter and leave the junction preferentially. Those electrons that enter the junction are strongly confined by the Lorentz potential, leading to various interference patterns. Moreover, for some parameters [see Fig. 11], we can observe extremely pronounced interference patterns inside the junction, such as whispering gallery modes [36,69,76]. These modes are an interference phenomenon of the electron waves confined in a potential well. It is interesting to see that such modes can

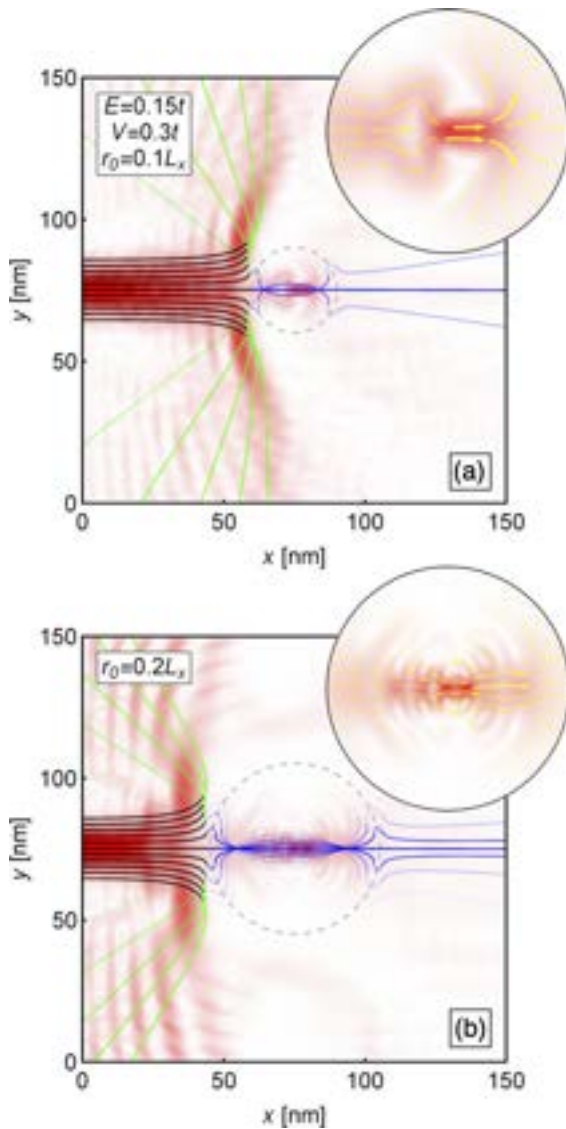


FIG. 10. Gradient-index electron optics in smooth circular p - n junctions ($\alpha = 2$). The dashed circle indicates the isoline $V(r) = E$. The current flow pattern and the semiclassical trajectories agree roughly. The differences can be explained by the existence of an energetically forbidden region, which enhances reflections outside the junction as well as the confinement inside the junction and hence leads to pronounced interference patterns. The interface of the forbidden region is indicated by the point where the trajectories change their color from black to green. The inset shows an enlargement close to the center of the p - n junction.

be induced by an external electron beam. These devices might find use as sensors of external electric or magnetic fields [77].

In Fig. 12, we study the transition from smooth to abrupt circular p - n junctions by increasing the parameter α in Eq. (5). When the junction profile becomes more abrupt, the current density is dispersed more strongly and the focusing point of the current moves away from the center of the junction [see Fig. 10(b)] toward the left edge of the junction [see Fig. 8(b)]. Moreover, interference patterns are observed inside the junction, which depend sensitively on the smoothness of the junction.

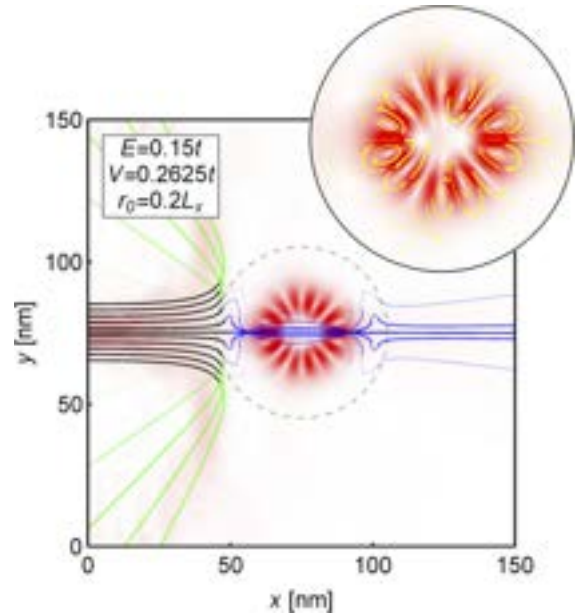


FIG. 11. Gradient-index electron optics in smooth circular p - n junctions. Strong interference patterns in the form of whispering gallery modes can be observed for specific parameters.

When studying smooth circular n - n' and p - p' junctions [see Fig. 13], we observe that the current flow patterns change qualitatively and more drastically in comparison with straight junctions [see Fig. 7]. In the n - n' regime, the Lorentz potential acts as a beam splitter, which separates even electrons

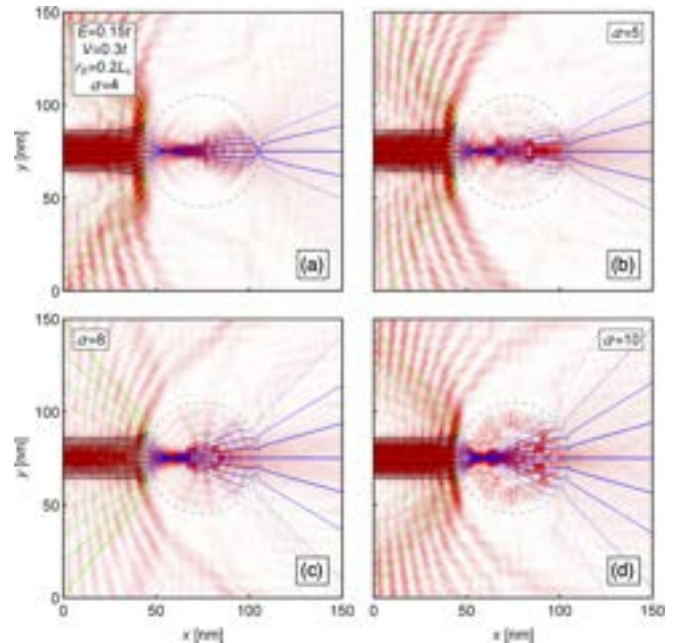


FIG. 12. Current flow in circular p - n junctions. When the parameter α is increased, the junction changes more abruptly. The current density is dispersed more strongly and the focusing point moves from the center of the junction [see Fig. 10(b)] toward the left [see Fig. 8(b)]. Moreover, distinct interference patterns can be observed inside the junction.

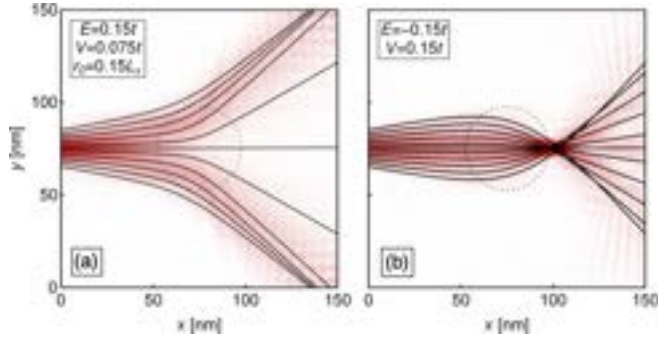


FIG. 13. Current flow in smooth circular n - n' (a) and p - p' (b) junctions. The former represent efficient electron beam splitters, while the latter act as a converging lens.

with small angular momentum. The semiclassical trajectories indicate that the Klein tunneling persists for zero angular momentum (normal incidence). Once more, the trajectories from Eq. (11) and numerical calculations of the current density show a remarkable agreement. Furthermore, a circular p - p' junction behaves like a converging lens; see Fig. 13(b). The electron current flow is focused on a single point behind the junction. In contrast with the p - n regime, interference patterns decrease, and therefore, p - p' and n - n' junctions are an ideal scenario to realize gradient-index electron optics. It is important to note that the refractive index defined by Eq. (8) is fully positive in the n - n' regime, while it is all negative in the p - p' regime. Moreover, we have demonstrated that the gradient-index electron optics is in line with the principles of light optics even for negative refraction, because “the rays bend towards the region of higher refractive index” [p. 132, 72]. Figure 14 shows the advantages of the optical methods used here over the relativistic geodesics. Apart from the classical regions where both approaches perfectly agree, we also see the tunneling through a forbidden region, corresponding to tracing the evanescent waves, and further propagation in a second classical region. In this way, we

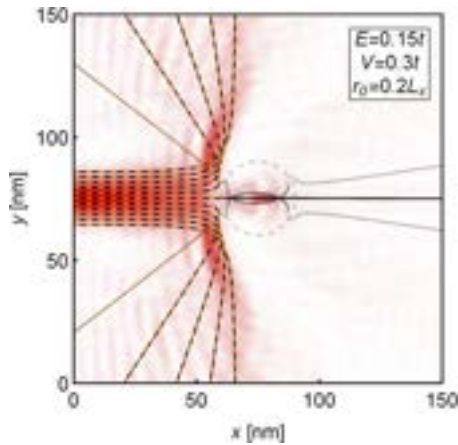


FIG. 14. Current flow in a smooth circular p - n junction. Semiclassical trajectories [see Eq. (11)] are shown by solid black curves, while the geodesics are given by the dashed orange curves. Both approaches are equivalent for the reflected electrons. However, geodesics cannot be used to estimate the paths of the electrons that are transmitted through the junction.

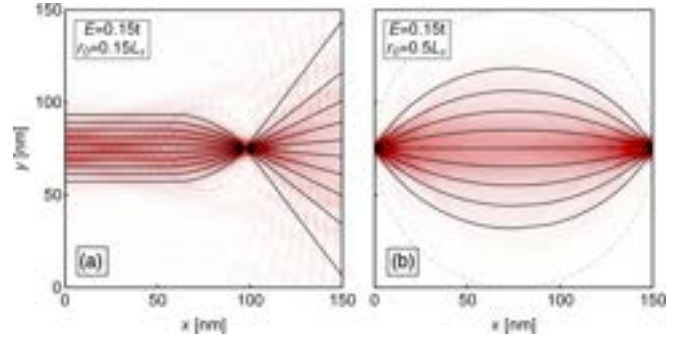


FIG. 15. Current flow in graphene with an electrostatic potential that generates a Luneburg lens (a) and a Maxwell's fish-eye lens (b).

obtain a much more complete picture and better agreement with the wave dynamics.

As a proof of principle, we also apply the developed techniques to the well-known Luneburg and Maxwell gradient-index lenses. The standard Luneburg lens [78] is known for its perfect focusing of parallel beams coming from any direction and is described by

$$n(r) = n_0 \begin{cases} \sqrt{2 - (r/r_0)^2} & \text{for } r < r_0 \\ 1 & \text{otherwise.} \end{cases} \quad (19)$$

In our situation, related to graphene, the interesting parameter is the potential $V(r)$ which follows from Eq. (8) and $n_0 = E/v_F$. The Maxwell's fish-eye lens [79] has all pairs of focusing points on a circle and is generated by the refractive index

$$n(r) = \frac{n_0}{1 + (r/r_0)^2}, \quad (20)$$

which is closely related to the previously used potential in Eq. (5). The functionality of these electron optical devices in graphene is demonstrated in Fig. 15. In the Luneburg lens [see Fig. 15(a)], the incoming parallel electron beam is focused onto a single point. In Maxwell's fish-eye lens [see Fig. 15(b)], a strongly diverging point source of electrons, injected at the left edge of the system, is refocused at the right edge. Both lenses can be used to control the current flow in graphene.

IV. CONCLUSIONS

In this paper, we investigated the ballistic current flow in smooth graphene p - n junctions. Comparing numerically calculated current densities with semiclassical trajectories, we demonstrated that the current flow in these devices can be understood largely in terms of gradient-index optics.

In straight p - n junctions, we confirmed the validity of a generalized Snell's law and reported additionally interference effects between the incident and reflected electron waves; see Figs. 4–6. Forbidden regions emerge in smooth junctions; see Fig. 3. The current is reflected at the interface of these regions, except for the normally incident electrons due to Klein tunneling. Such smooth p - n junctions can be used to generate narrow parallel electron beams.

In circular p - n junctions with an abruptly changing profile, the part of the current density that enters the junction is focused onto a single point, which agrees with a caustic of

the semiclassical trajectories; see Fig. 8. When the profile of the junction is smoothed, a circular junction with a gradually changing refractive index is obtained. The semiclassical trajectories agree qualitatively with the quantum current density but an energetically forbidden region intensifies the interference both outside and inside the junction; see Fig. 10. This strong interference in smooth circular p - n junction leads, for specific parameters, to interesting patterns such as whispering gallery modes; see Fig. 11. Finally, we demonstrated in Fig. 13 that smooth circular n - n' and p - p' junctions act as beam splitters and converging lenses, respectively. In Fig. 15, we proved the feasibility of realizing Luneberg and Maxwell lenses in graphene.

The semiclassical trajectories are an efficient tool to estimate the current flow in nanoelectronic devices. They are valid in the regime where the Fermi wavelength of the electrons is much larger than the lattice constant but smaller than the characteristic lengths appearing in the system (for example, the width of the interface of a p - n junction) in order to resolve them. These restrictions can be summarized as

$$\text{lattice constant} \ll \text{electron wavelength} \ll \text{characteristic length scales.}$$

In contrast, the NEGF simulations are necessary when the electron waves create strong interference patterns which cannot be cast by the semiclassical methods.

We are confident that the presented broad variety of different properties of smooth graphene p - n junctions will stimulate gradient-index optics experiments in graphene. Our findings contribute to the overall understanding of the local current flow in graphene and may eventually lead to new nanoelectronic devices.

ACKNOWLEDGMENTS

E.P.-R. gratefully acknowledges a CONACYT graduate scholarship. E.P.-R. thanks N. Szpak and D. Wolf for their hospitality at the University Duisburg-Essen (Germany), where part of this research was performed. E.P.-R., Y.B.-O., and T.S. gratefully acknowledge funding from CONACYT Proyecto Fronteras 952, CONACYT Proyecto A1-S-13469, and UNAM-PAPIIT IA103020. N.S. gratefully acknowledges funding by the Deutsche Forschungsgemeinschaft (DFG, German Research Foundation), Project No. 278162697, SFB 1242.

-
- [1] G.-H. Lee, G.-H. Park, and H.-J. Lee, *Nat. Phys.* **11**, 925 (2015).
 - [2] J. Cayssol, B. Huard, and D. Goldhaber-Gordon, *Phys. Rev. B* **79**, 075428 (2009).
 - [3] J. R. Williams, T. Low, M. S. Lundstrom, and C. M. Marcus, *Nat. Nanotechnol.* **6**, 222 (2011).
 - [4] B. Brun, N. Moreau, S. Somanchi, V.-H. Nguyen, K. Watanabe, T. Taniguchi, J.-C. Charlier, C. Stampfer, and B. Hackens, *Phys. Rev. B* **100**, 041401(R) (2019).
 - [5] J. Cserti, A. Pályi, and C. Péterfalvi, *Phys. Rev. Lett.* **99**, 246801 (2007).
 - [6] V. V. Cheianov, V. Fal'ko, and B. L. Altshuler, *Science* **315**, 1252 (2007).
 - [7] J. L. Garcia-Pomar, A. Cortijo, and M. Nieto-Vesperinas, *Phys. Rev. Lett.* **100**, 236801 (2008).
 - [8] P. E. Allain and J. N. Fuchs, *Eur. Phys. J. B* **83**, 301 (2011).
 - [9] A. F. Young and P. Kim, *Nat. Phys.* **5**, 222 (2009).
 - [10] S. Chen, Z. Han, M. M. Elahi, K. M. M. Habib, L. Wang, B. Wen, Y. Gao, T. Taniguchi, K. Watanabe, J. Hone *et al.*, *Science* **353**, 1522 (2016).
 - [11] B. Huard, J. A. Sulpizio, N. Stander, K. Todd, B. Yang, and D. Goldhaber-Gordon, *Phys. Rev. Lett.* **98**, 236803 (2007).
 - [12] A. H. Castro Neto, F. Guinea, N. M. R. Peres, K. S. Novoselov, and A. K. Geim, *Rev. Mod. Phys.* **81**, 109 (2009).
 - [13] K.-K. Bai, J.-J. Zhou, Y.-C. Wei, J.-B. Qiao, Y.-W. Liu, H.-W. Liu, H. Jiang, and L. He, *Phys. Rev. B* **97**, 045413 (2018).
 - [14] X. Zhou, A. Kerelsky, M. M. Elahi, D. Wang, K. M. M. Habib, R. N. Sajjad, P. Agnihotri, J. U. Lee, A. W. Ghosh, F. M. Ross *et al.*, *ACS Nano* **13**, 2558 (2019).
 - [15] J. Hu, A. F. Rigosi, J. U. Lee, H.-Y. Lee, Y. Yang, C.-I. Liu, R. E. Elmquist, and D. B. Newell, *Phys. Rev. B* **98**, 045412 (2018).
 - [16] K.-K. Bai, J.-B. Qiao, H. Jiang, H. Liu, and L. He, *Phys. Rev. B* **95**, 201406(R) (2017).
 - [17] M. I. Katsnelson, K. S. Novoselov, and A. K. Geim, *Nat. Phys.* **2**, 620 (2006).
 - [18] V. V. Cheianov and V. I. Fal'ko, *Phys. Rev. B* **74**, 041403(R) (2006).
 - [19] N. Stander, B. Huard, and D. Goldhaber-Gordon, *Phys. Rev. Lett.* **102**, 026807 (2009).
 - [20] D. Schurig, J. J. Mock, B. J. Justice, S. A. Cummer, J. B. Pendry, A. F. Starr, and D. R. Smith, *Science* **314**, 977 (2006).
 - [21] J. B. Pendry, *Phys. Rev. Lett.* **85**, 3966 (2000).
 - [22] V. G. Veselago, *Sov. Phys. Usp.* **10**, 509 (1968).
 - [23] N. Levy, S. A. Burke, K. L. Meaker, M. Panlasigui, A. Zettl, F. Guinea, A. H. Castro Neto, and M. F. Crommie, *Science* **329**, 544 (2010).
 - [24] F. Guinea, M. I. Katsnelson, and A. K. Geim, *Nat. Phys.* **6**, 30 (2010).
 - [25] T. Low and F. Guinea, *Nano Lett.* **10**, 3551 (2010).
 - [26] T. Stegmann and N. Szpak, *New J. Phys.* **18**, 053016 (2016).
 - [27] B. Amorim, A. Cortijo, F. de Juan, A. Grushin, F. Guinea, A. Gutiérrez-Rubio, H. Ochoa, V. Parente, R. Roldán, P. San-Jose *et al.*, *Phys. Rep.* **617**, 1 (2016).
 - [28] G. G. Naumis, S. Barraza-Lopez, M. Oliva-Leyva, and H. Terrones, *Rep. Prog. Phys.* **80**, 096501 (2017).
 - [29] R. L. Heinisch, F. X. Bronold, and H. Fehske, *Phys. Rev. B* **87**, 155409 (2013).
 - [30] Y. Betancur-Ocampo, *J. Phys.: Condens. Matter* **30**, 435302 (2018).
 - [31] Y. Betancur-Ocampo, *Phys. Rev. B* **98**, 205421 (2018).
 - [32] W. Mu, G. Zhang, Y. Tang, W. Wang, and Z. Ou-Yang, *J. Phys.: Condens. Matter* **23**, 495302 (2011).
 - [33] C. Péterfalvi, A. Pályi, and J. Cserti, *Phys. Rev. B* **80**, 075416 (2009).
 - [34] S. Prabhakar, R. Nepal, R. Melnik, and A. A. Kovalev, *Phys. Rev. B* **99**, 094111 (2019).
 - [35] N. A. Garg, S. Ghosh, and M. Sharma, *J. Phys.: Condens. Matter* **26**, 155301 (2014).

- [36] Y. Jiang, J. Mao, D. Moldovan, M. R. Masir, G. Li, K. Watanabe, T. Taniguchi, F. M. Peeters, and E. Y. Andrei, *Nat. Nanotechnol.* **12**, 1045 (2017).
- [37] A. Mreńca-Kolasińska, S. Heun, and B. Szafran, *Phys. Rev. B* **93**, 125411 (2016).
- [38] M. A. Khan and M. N. Leuenberger, *Phys. Rev. B* **90**, 075439 (2014).
- [39] T. Stegmann and N. Szpak, *2D Mater.* **6**, 015024 (2018).
- [40] F. Zhai, Y. Ma, and K. Chang, *New J. Phys.* **13**, 083029 (2011).
- [41] D. Zhai and N. Sandler, *Phys. Rev. B* **98**, 165437 (2018).
- [42] M. M. Grujić, M. Z. Tadić, and F. M. Peeters, *Phys. Rev. Lett.* **113**, 046601 (2014).
- [43] J. R. Schaibley, H. Yu, G. Clark, P. Rivera, J. S. Ross, K. L. Seyler, W. Yao, and X. Xu, *Nat. Rev. Mater.* **1**, 16055 (2016).
- [44] M. Settnes, J. H. Garcia, and S. Roche, *2D Mater.* **4**, 031006 (2017).
- [45] M. Settnes, S. R. Power, M. Brandbyge, and A.-P. Jauho, *Phys. Rev. Lett.* **117**, 276801 (2016).
- [46] S. P. Milovanović and F. M. Peeters, *Appl. Phys. Lett.* **109**, 203108 (2016).
- [47] R. Carrillo-Bastos, M. Ochoa, S. A. Zavala, and F. Mireles, *Phys. Rev. B* **98**, 165436 (2018).
- [48] R. Carrillo-Bastos, C. León, D. Faria, A. Latgé, E. Y. Andrei, and N. Sandler, *Phys. Rev. B* **94**, 125422 (2016).
- [49] P. Rickhaus, P. Makk, K. Richter, and C. Schönenberger, *Appl. Phys. Lett.* **107**, 251901 (2015).
- [50] J. J. Wang, S. Liu, J. Wang, and J.-F. Liu, *Phys. Rev. B* **98**, 195436 (2018).
- [51] C.-H. Park, Y.-W. Son, L. Yang, M. L. Cohen, and S. G. Louie, *Nano Lett.* **8**, 2920 (2008).
- [52] M.-H. Liu, C. Gorini, and K. Richter, *Phys. Rev. Lett.* **118**, 066801 (2017).
- [53] R. N. Sajjad and A. W. Ghosh, *Appl. Phys. Lett.* **99**, 123101 (2011).
- [54] D. Gunlycke and C. T. White, *Phys. Rev. B* **90**, 035452 (2014).
- [55] H. Graef, Q. Wilmart, M. Rosticher, D. Mele, L. Banszerus, C. Stampfer, T. Taniguchi, K. Watanabe, J.-M. Berroir, E. Bocquillon *et al.*, *Nat. Commun.* **10**, 2428 (2019).
- [56] K. Wang, M. M. Elahi, L. Wang, K. M. M. Habib, T. Taniguchi, K. Watanabe, J. Hone, A. W. Ghosh, G.-H. Lee, and P. Kim, *Proc. Nat. Acad. Sci. USA* **116**, 6575 (2019).
- [57] Q. Wilmart, S. Berrada, D. Torrin, V. H. Nguyen, G. Fève, J.-M. Berroir, P. Dollfus, and B. Plaçais, *2D Mater.* **1**, 011006 (2014).
- [58] P. Bøggild, J. M. Caridad, C. Stampfer, G. Calogero, N. R. Papior, and M. Brandbyge, *Nat. Commun.* **8**, 15783 (2017).
- [59] Y. Betancur-Ocampo, F. Leyvraz, and T. Stegmann, *Nano Lett.* **19**, 7760 (2019).
- [60] Y. Betancur-Ocampo, E. Paredes-Rocha, and T. Stegmann, *J. Appl. Phys.* **128**, 114303 (2020).
- [61] R. D. Y. Hills, A. Kusmartseva, and F. V. Kusmartsev, *Phys. Rev. B* **95**, 214103 (2017).
- [62] M. Yang, Q.-T. Hou, and R.-Q. Wang, *New J. Phys.* **21**, 113057 (2019).
- [63] M. Yang, Q.-T. Hou, and R.-Q. Wang, *New J. Phys.* **22**, 033015 (2020).
- [64] M. Lu and X.-X. Zhang, *J. Phys.: Condens. Matter* **30**, 215303 (2018).
- [65] S.-H. Zhang and W. Yang, *New J. Phys.* **21**, 103052 (2019).
- [66] L. Cohnitz, A. De Martino, W. Häusler, and R. Egger, *Phys. Rev. B* **94**, 165443 (2016).
- [67] J.-S. Wu and M. M. Fogler, *Phys. Rev. B* **90**, 235402 (2014).
- [68] B. Liao, M. Zebajadi, K. Esfarjani, and G. Chen, *Phys. Rev. B* **88**, 155432 (2013).
- [69] Y. Zhao, J. Wyrick, F. D. Natterer, J. F. Rodriguez-Nieva, C. Lewandowski, K. Watanabe, T. Taniguchi, L. S. Levitov, N. B. Zhitenev, and J. A. Stroscio, *Science* **348**, 672 (2015).
- [70] B. Brun, N. Moreau, S. Somanchi, V.-H. Nguyen, A. Mreńca-Kolasińska, K. Watanabe, T. Taniguchi, J.-C. Charlier, C. Stampfer, and B. Hackens, *2D Mater.* **7**, 025037 (2020).
- [71] R. N. Sajjad, S. Sutar, J. U. Lee, and A. W. Ghosh, *Phys. Rev. B* **86**, 155412 (2012).
- [72] M. Born and E. Wolf, *Principles of Optics* (Cambridge University Press, Cambridge, UK, 1999).
- [73] S. Datta, *Electronic Transport in Mesoscopic Systems* (Cambridge University Press, Cambridge, UK, 1997).
- [74] S. Datta, *Quantum Transport: Atom to Transistor* (Cambridge University Press, Cambridge, UK, 2005).
- [75] T. Low, S. Hong, J. Appenzeller, S. Datta, and M. S. Lundstrom, *IEEE Trans. Electron Devices* **56**, 1292 (2009).
- [76] F. Ghahari, D. Walkup, C. Gutiérrez, J. F. Rodriguez-Nieva, Y. Zhao, J. Wyrick, F. D. Natterer, W. G. Cullen, K. Watanabe, T. Taniguchi *et al.*, *Science* **356**, 845 (2017).
- [77] M. R. Foreman, J. D. Swaim, and F. Vollmer, *Adv. Opt. Photon.* **7**, 168 (2015).
- [78] R. K. Luneberg, *Mathematical Theory of Optics* (Brown University, Providence, RI, 1944), pp. 189–213.
- [79] J. C. Maxwell, *Cambridge Dublin Math. J.* **9**, 9 (1854).